RSC Advances

PAPER

View Article Online
View Journal | View Issue

Check for updates

Cite this: *RSC Adv.*, 2022, **12**, 20454

Enhanced dielectric properties of polystyrene by using graphene incorporated styrene-butyl acrylate microspheres

Zhaoyang Zhang,[a] Gan Tang,[a] Feng You,*[ac] Xueliang Jiang,[a] Chu Yao,[a] Ruofei Hu,*[b] Junlong Yao[a] and Pei Zhao[a]

Received 2nd June 2022
Accepted 6th July 2022

DOI: 10.1039/d2ra03427a

rsc.li/rsc-advances

In view of the current trend of capacitor materials, the development of capacitors with high dielectric permittivity and low dielectric loss is of great interest. In this work, the dielectric permittivity of reduced graphene oxide-incorporated styrene-butyl acrylate (rGO@SBA) composite microspheres synthesized by mini-emulsion polymerization was significantly improved. rGO with 2 wt% content gave a dielectric permittivity of 11 356 (at 1 KHz), which was 1925 times higher than that of pure SBA (5.9). SEM and TEM were conducted to observe the morphology and structure of the composite microspheres. After filling into polystyrene (PS), a segregated structure of (rGO@SBA) that enables a concentrated aggregation of rGO in SBA was fabricated. The dielectric permittivity of PS could reach 10.91 (at 1 KHz) by incorporating only 0.39 wt% rGO by using this segregated structure of (rGO@SBA). PS simply mixed with SBA microspheres and graphite (PS/rGO-SBA) was also fabricated as a comparison group to verify the effect of this segregated structure on the dielectric properties of the composites. After comparing the dielectric properties of PS composites with different structures, the enhancement in dielectric permittivity of the composites can be demonstrated.

Introduction

With the development of electronic technology, the demand for dielectric materials with high energy storage has become increasingly urgent.[1–3] For filled dielectric materials, ferroelectric ceramic fillers and conductive particulate fillers are usually added to the matrix to obtain high dielectric polymer matrix composites.[4,5] Among them, the ferroelectric ceramic-type filler tends to agglomerate when it is compounded with a high-viscosity polymer matrix due to its high surface energy, resulting in inhomogeneous dispersion. At the same time, this filler has no organic functional groups on its surface and interacts poorly with the matrix, thus leading to defects such as holes and cracks in the prepared materials.[6,7] The conductive filler (*e.g.* carbon nanotubes,[8,9] graphene,[10–12] conductive oxides,[13] metal nanoparticles,[14,15] *etc.*) filled dielectric materials also face an important problem: the leakage current caused by the polarization of the filler increases the leakage current and thus increases the dielectric loss.[16–18] In the work of Ni *et al.*, sulfated GO was filled with cyanate (CE), and the results indicated that although the dielectric permittivity was enhanced somewhat by the conductive filler GO, the dielectric loss tangent remained high at the same time (reaching 150, at 25 wt% filling content and 1 KHz).[19]

Many researchers have devoted to develop new filler structures to reduce dielectric loss.[20,21] Of these, the core–shell structure is undoubtedly of paramount importance.[22–24] This core–shell structure has been demonstrated to constrain the leakage current of the composite during interfacial polarization and thus effectively reduce interfacial losses. Lu *et al.* designed a novel composite filler with a core–shell structure, using tetrapodal zinc oxide whiskers (T-ZnOw) as the core, two-dimensional graphene oxide (GO) as the shell, and polydopamine (PDA) as the adhesion layer, enabling this composite structure GO/PDA@T-ZnOw to be uniformly dispersed in polyvinylidene fluoride (PVDF).[25] After filled with 2 wt% of the composite filler, the dielectric permittivity can be as high as 104 at a frequency of 100 Hz with a dielectric loss tangent as low as 1. The mechanism is mainly ascribed to the construction of multiple interfaces in the composite, providing more probability of interface polarization in electric field to promote dipole or charge migration from GO platelets to T-ZnOw. Zhang *et al.* investigated the effect of metal–semiconductor Zn–ZnO core–shell structure on the dielectric properties of polyvinylidene fluoride (PVDF) composites.[26] Their results demonstrated that Zn–ZnO/PVDF composites have higher dielectric permittivity than that of Zn/PVDF composites. This can be attributed to

---

[a] Hubei Key Laboratory of Plasma Chemistry and New Materials, School of Material Science and Engineering, Wuhan Institute of Technology, Wuhan, 430205, China

[b] Department of Food Science & Chemical Engineering, Hubei University of Arts and Science, Xiangyang, 441053, China. E-mail: rhuvip@hbuas.edu.cn

[c] Foshan (Southern China) Institute for New Materials, Foshan, 528200, Guangdong, China. E-mail: Youfeng.mse@wit.edu.cn

duplex interfacial polarizations induced by metal–semiconductor interface and semiconductor–insulator interface. Liang *et al.* prepared a composite material by embedding a core–shell Ag@TiO_2 filler in polytetrafluoroethylene (PTFE).[27] Ag nanoparticles were homogeneously coated with TiO_2 to give a shell thickness of approximately 810 nm. The composite contained Ag@TiO_2 nanoparticles with rutile shells exhibited better dielectric properties than that of the composite containing Ag@TiO_2 nanoparticles with anatase shells. The relative dielectric constant of the composite containing 70 vol% filler was approximately 240 at 100 Hz, which was increased more than 100 times higher than that of pure PTFE.

In addition to the filler structure, the fabrication methods of the composite also affect its dielectric properties.[28,29] Chao *et al.* prepared $CaCu_3Ti_4O_{12}$ (CCTO) particles by the sol–gel (sg) and solid-state (ss) methods,[30] respectively. The CCTO obtained by the sg method was more uniformly distributed with a particle size of about 480 nm, which im-proved the dielectric constant of the composite due to its stable chemical activation and lower crystallization temperature. Furthermore, the dielectric constant of the CCTO-sg/PVDF composites reached 62.3 at 100 Hz when the CCTO-sg content was 50 wt%. The dielectric constant of the CCTO-sg/PVDF composites was twice as high as that of the CCTO-ss/PVDF composites with the same filler content.

In this work, rGO-incorporated SBA (rGO@SBA) composite microspheres were obtained by a mini-emulsion polymerization technique to significantly improve the dielectric constant of polystyrene (10.91 at 1 KHz) while still maintaining a low dielectric loss tangent. rGO and SBA directly filled polystyrene were also fabricated as a comparison group to study the effect of this composite microsphere structure on the dielectric properties of polystyrene. The effects of different structures of rGO on the dielectric properties of polystyrene are discussed in detail.

Experimental

Materials

Graphite (300 mesh), styrene (St), butyl acrylate (BA), sodium dodecyl sulfate (SDS), potassium persulfate (KPS) and phosphoric acid were purchased from Sinopharm Chemical Reagents (China); Hydrazine hydrate was purchased from Beijing Chemical Factory (China); 2-acrylamido-2-methylpropanesulfonic (AMPS) was purchased from Aladdin Reagents Ltd (China); Polystyrene (PS 666D), melt flow index = 8.0 g (10 min^{-1}) was obtained from RTP (USA).

Fabrication of rGO@SBA composite microspheres

Step 1: before mini-emulsion polymerization, styrene and butyl acrylate monomer were purified with NaOH solution (25 wt%) in a separatory funnel to remove inhibitor. GO was prepared by a modified Hummers' method.[31] Typically, a quantitative amount of GO and deionized water is weighed and poured into a three-necked flask according to Table 1 and sonicated for 2 h to obtain a homogeneous GO dispersion. 5 ml of hydrazine hydrate was slowly poured in and the reaction was carried out at 95 °C for 12 h to obtain the rGO dispersion. The AMPS-treated rGO dispersion was obtained by adding the corresponding amount of AMPS and stirred at room temperature for 24 h.

Table 1 The dosage of each component during the fabrication of rGO@SBA

Mass fraction of rGO (wt%)	St (g)	BA (g)	GO (g)	AMPS (g)
0.4	36	4	0.156	0.124
0.8	36	4	0.312	0.250
1.2	36	4	0.468	0.374
2	36	4	0.800	0.640
3	36	4	1.200	0.960
4	36	4	1.600	1.280

Step 2: as shown in Table 1, the corresponding amounts of purified styrene and butyl acrylate were weighed into the dispersion and mixed, SDS and deionized water were added and sonicated to obtain a homogeneous mini emulsion. After the addition of KPS, the rGO@SBA mini emulsion was obtained by reacting at 70 °C for 5 h under nitrogen protection. rGO@SBA powder was obtained by freeze-drying for 48 h.

Fabrication of PS/rGO@SBA composite microspheres

To ensure the comparability of the two preparation methods, the mass fractions of matrix and filler were uniformly set as 87 wt% and 13 wt%. And the effect on the dielectric properties was investigated by adjusting the mass ratio of rGO in the filler (0, 0.05 and 0.39 wt%). After placed the composites in a self-made mold and heated above the melting temperature (160 °C). Preheated for 10 min, hold pressure at 15 MPa for 5 min, and cold press for 5 min to fabricate the PS/rGO@SBA and PS/rGO-SBA composites.

Characterization

A scanning electron microscope (SEM, JSM-5510) with an accelerating voltage of 20 kV was used to observe the morphologies of rGO@SBA composite microspheres, PS/rGO@SBA and PS/rGO-SBA. Transmission electron microscope (TEM, JEM-2100) images were taken with a JEOL microscope operating at 15 kV. The particle size distribution of rGO@SBA composite microspheres, SBA was obtained by using a PSS particle sizer (380ZLS, USA). The number-averaged diameter (D_i) was calculated by eq. below.

$$D_a = \frac{\sum_i N_i D_i}{\sum_i D_i}$$

where N_i is the number of particles with a diameter of D_i. Fourier transform infrared spectroscopy (FTIR, Thermal Electron Nicolet6700) was used to obtain the infrared transmittance of the samples. The Raman sperctra of GO and rGO powder were collected by using Raman spectrometer (Invia, UK). The dielectric properties were obtained by Agilent 4294A impedance analyzer in a frequency region of 10^3–10^7 Hz.

Results and discussion

Morphology and structure of rGO@SBA composite microspheres

Scheme 1 illustrates the synthesis of segregated PS/rGO@SBA fabricated by mini-emulsion polymerization and other PS/rGO-SBA without segregated structure and simulates the structure of the microspheres. By arranging the composite material in a mold and applying a certain pressure, a block specimen of the desired thickness is prepared. In PS/rGO@SBA, the structure in which rGO@SBA microspheres were segregated from each other by the PS matrix are simulated. This structure can also be verified from the SEM images in the following text.

Fig. 1 shows the FTIR of GO, rGO, SBA and rGO (0.39 wt%) @SBA. As shown in the figure, the peaks at 3429 cm^{-1} and 1740 cm^{-1} on the GO curve correspond to the stretching vibration peaks of –OH and C=O. The peak at 1630 cm^{-1} is generated by the bending vibration of C–OH, and these prove that GO contains oxygen-functional groups such as hydroxyl and carboxyl groups. In the spectrum of rGO, we found that the oxygen-containing functional groups present in GO were substantially removed, which is an important proof of the reduction of GO. For SBA, 2930 cm^{-1} and 1600 cm^{-1} correspond to the stretching vibration peaks of the benzene ring backbone generated by the styrene segment, respectively. 1730 cm^{-1} and 1160 cm^{-1} are C=O and C–O stretching vibration peaks produced by acrylate segments, which indicate that the mini-emulsion polymerization has successfully prepared SBA microspheres. Lastly, the partial features of SBA and rGO preserved on the rGO@SBA composite microspheres spectrum. The above conclusions can prove the successful preparation of rGO@SBA composite microspheres. Fig. 1(b) shows the Raman spectra of GO and rGO. It can be observed that the Raman spectra of both samples show obvious double peaks, in which the peaks near 1350 (D band) and 1595 (G band) cm^{-1} are corresponded to the carbon atoms of sp^3 and sp^2 hybridization, respectively. The ratio of D-peak intensity to G-peak intensity is defined as *R*-value, and the magnitude of *R*-value reflects the degree of functionalization and integrity of the graphene structure; the larger the *R*-value is, the more sp^3-hybridized carbon atoms are in the graphene structure, and the more severely the graphene structure is damaged. The *R*-values of GO and rGO were calculated as 1.04 and 1.19, respectively. The larger *R* value of rGO also demonstrates that GO was successfully reduced.

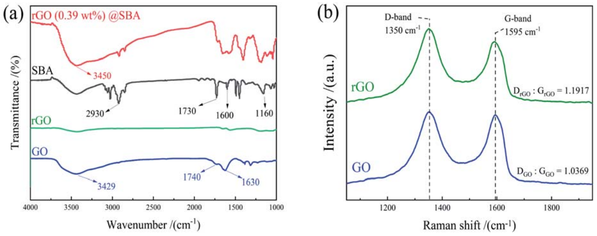

Fig. 1 (a) FTIR of GO, rGO, SBA and rGO @SBA. (b) Raman spectra of GO and rGO.

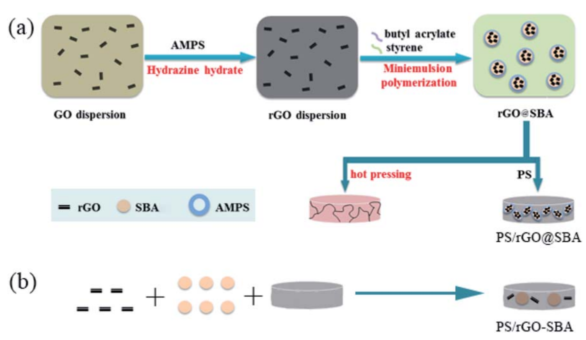

Scheme 1 Fabrication of (a) PS/rGO@SBA and (b) PS/rGO-SBA composites.

Fig. 2 shows the morphology and structure of SBA and rGO (0.39 wt%) @SBA microspheres. Fig. 2(a) is the SEM image of SBA composite microspheres which shows a smooth surface with uniform distribution and no visible aggregation, indicating that the SBA can be synthesized by the mini-emulsion polymerization method. Fig. 2(b) shows the SEM photo of the rGO incorporated microspheres, the surface of the rGO (0.39 wt%) @SBA microspheres are rough due to the APMS as surfactant wrapped in the surface layer of rGO@SBA. Composite microspheres. The illustrated core–shell structure mechanism of rGO@SBA composite microspheres in Fig. 2(d) corresponds to the shaded part of the TEM image in Fig. 2(c). It can be found that an obvious shell layer is coated on the surface of microspheres. In addition, the wrinkled rGO nanosheets could be seen in the core of microspheres, implying rGO has been successfully embedded to SBA microspheres. On the other hand, the particle size distribution of SBA and rGO (0.39 wt%) @SBA measured by PSS particle size analyzer are shown in Fig. 2(e) and (f). After incorporated with rGO, the average particle size of SBA microspheres increased from 56.7 nm to 106.3 nm.

Dielectric properties of rGO@SBA composites

Fig. 3(a) shows the frequency dependence of the dielectric constant of rGO@SBA composite with different rGO contents. The dielectric content of rGO@SBA increases with the rGO content increased, reaching 11 356 (at 1 KHz) when the rGO content reaches 2 wt%, which is 1925 times higher than that of pure SBA. This was due to the high electrical conductivity of rGO, as the rGO content increased, the number of electric dipoles in the system increased, and when they accumulated to a certain number, a conductive pathway formed between the nanoparticles. The dielectric constant tends to decrease as the frequency increases. This is because the electric dipole tends to move in the direction of the external electric field under the action of the external electric field. In the high frequency region, the electric field direction changes rapidly, so that the electric dipole does not gather more in the direction of the electric field, and therefore the polarization by the charge accumulation decreases, leading to a decrease in its dielectric constant. The dielectric loss tangent of rGO@SBA composites with rGO

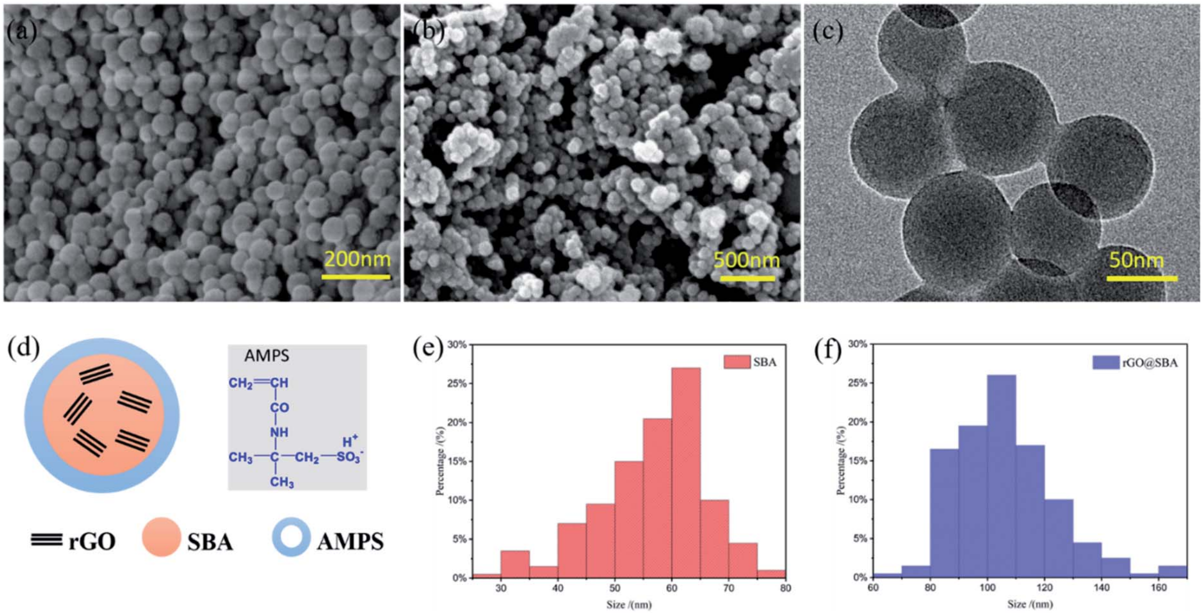

Fig. 2 SEM images of (a) neat SBA and (b) rGO (0.39 wt%) @SBA, TEM image of (c) rGO (0.39 wt%) @SBA; (d) simulated structure of rGO@SBA, (e and f) statistical SBA and rGO (0.39 wt%)@SBA particle size distribution.

content and frequency is shown in Fig. 3(b). When an external electric field is applied, the electric dipole in the rGO@SBA composites will produce local movement, a process that requires work to overcome friction, consuming some electrical energy and converting it into heat, resulting in dielectric loss. As the amount of rGO increases, the dielectric loss tangent also increases gradually. When its amount reached the percolation threshold (2 wt%), the conductive path formed between rGO and rGO will generate a large leakage conduction current, resulting in a large loss of electron polarization, which increases the dielectric loss tangent of rGO@SBA composites to 591.2 (at 1 KHz), while the tangent of pure SBA is only 0.058. The dielectric loss tangent of rGO@SBA composites has a greater dependence on frequency because the charge in the system is easy to migrate in the low frequency stage, and more heat is generated, which makes the dielectric loss tangent in this stage larger; when the frequency increases, the charge transfer is limited, so dielectric loss tangent in this band (10^4–10^7 Hz) are hardly affected by frequency changes. The conductivity of rGO@SBA composites under different rGO content and frequency is shown in Fig. 3(c). The conductivity of rGO@SBA increases with the increase of rGO, after filled with 2 wt% rGO, the conductivity of rGO@SBA is 0.08 S cm^{-1} (at 1 KHz). When the filling amount is greater than 2 wt%, the conductivity of rGO@SBA tends to be stable, at this time rGO@SBA can already be applied as a conductive material.

Effects of different fabrication methods of rGO and SBA on the dielectric properties of PS

To explore the impact mechanism of rGO@SBA composite microspheres on the dielectric properties, the following comparison test were designed. The SBA obtained by mini-emulsion polymerization and rGO were separately added to the PS matrix to prepare PS/rGO-SBA composites. The fabrication method is shown in Scheme 1b.

Fig. 4 shows the relationship between the dielectric properties and frequency of PS composites prepared by different

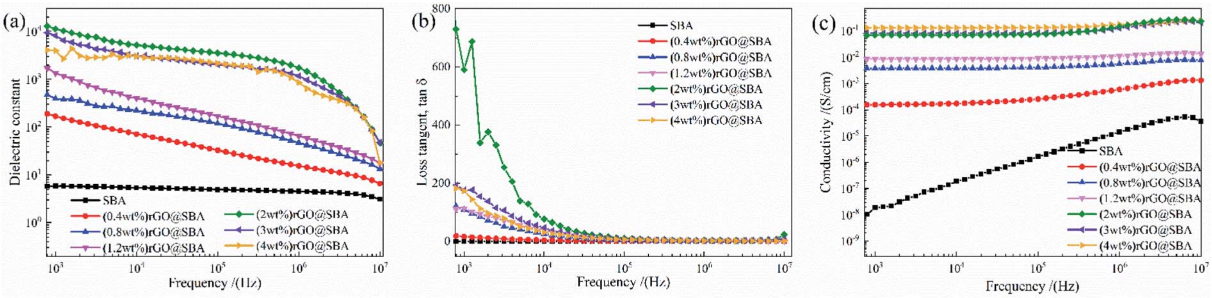

Fig. 3 (a) Dielectric constant and (b) loss tangent of rGO@SBA at different rGO contents and frequencies. (c) Frequency dependence of the electrical conductivity of rGO@SBA.

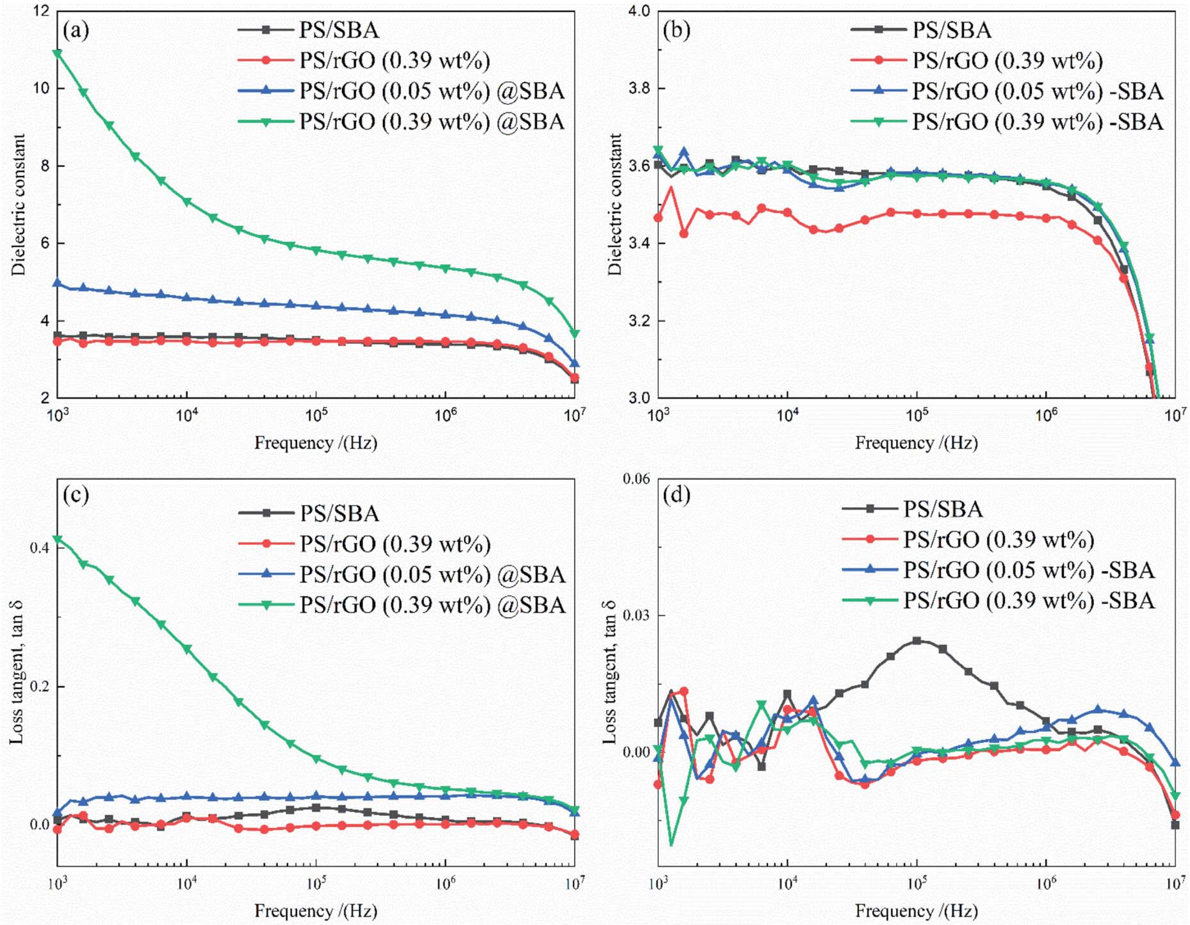

Fig. 4 Dielectric constant of (a) PS/rGO@SBA composites and (b) PS/rGO-SBA at different frequencies, loss tangent of (c) PS/rGO@SBA composites and (d) PS/rGO-SBA at different frequencies.

methods at different frequency. The dielectric constant curves of PS/rGO@SBA composites with segregated structure under different rGO contents are shown in Fig. 4(a). In the rGO@SBA structure, the dielectric properties of PS/rGO@SBA increased with increasing rGO content, with the highest dielectric constant of 10.91 (at a frequency of 1 KHz) at 0.39 wt% rGO content, which is 3.28 times higher than that of pure PS (3.33). In contrast, the dielectric constant of PS/rGO did not change significantly under the same rGO filling amount (0.39 wt%). This was since the segregated structures that rGO@SBA formed in the PS matrix, and this structure facilitated the formation of micro-capacitors, which favors the dielectric constant. To provide more favorable evidence, we prepared PS composites directly filled with rGO and SBA without the segregation structure and their dielectric constants are shown in Fig. 4(b). Although the rGO content increased to 0.39%, the dielectric constants did not increase significantly. Combining this result with Table 2 can more effectively proves that the segregated structure is more effective in improving the dielectric properties of the composite. Fig. 4(c) shows the frequency dependence of the loss tangent of PS/rGO@SBA composites with different rGO contents. The frequency dependence of the dielectric loss tangent is higher for the PS/rGO (0.39 wt%)@SBA composites. At a frequency of 1 KHz, the loss tangent of the composite is 0.41. At this point, the rGO content reaches the percolation threshold and a large leakage current generated during the polarization of the composite, leading to an increasement in its loss tangent. The frequency dependence of the loss tangent of the PS/rGO-SBA composite at different rGO contents is shown in Fig. 4(d), where the tangent of the composites at different frequencies did not change significantly when the rGO content

Table 2 Effects of different fabrication methods of rGO and SBA on the dielectric properties of PS composites

	rGO content (wt%) in SBA	
Sample (at 1 KHz)	0.00	0.39
Dielectric constant		
PS/rGO@SBA	3.60	10.91
PS/rGO-SBA	3.60	3.64
PS/rGO	3.33	3.47
Loss tangent		
PS/rGO@SBA	0.007	0.413
PS/rGO-SBA	0.007	0.001
PS/rGO	0.015	0.007

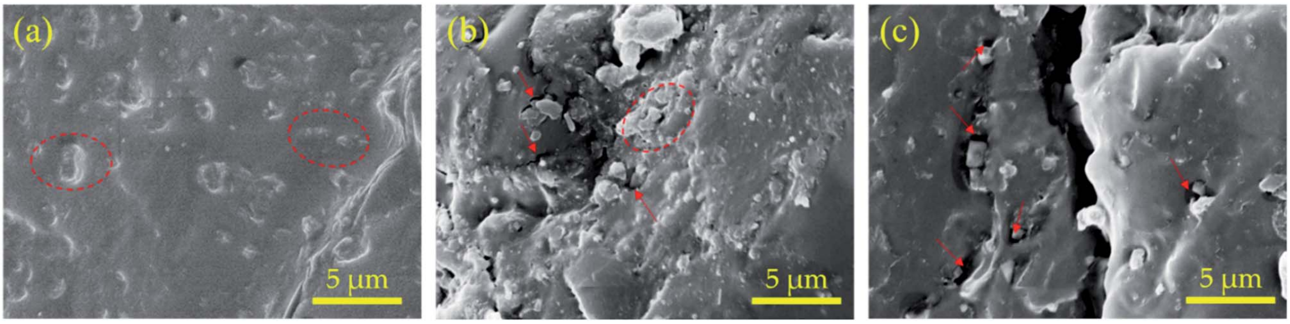

Fig. 5 Morphology of (a) PS/rGO (0.39 wt%)@SBA, (b) PS/rGO (0.39 wt%)-SBA, (c) PS/rGO (0.39 wt%) composite.

increased nor the PS/rGO@SBA composites with a segregated structure can be significantly enhanced while maintaining a low dielectric loss tangent.

Morphology of different PS composites

To visualize the morphology of the different structures of the composite, a cross-sectional morphological characterization was carried out. It can be observed that the filler particles are uniformly sized and evenly distributed in the matrix (as shown in the dashed circles in the Fig. 5(a)). Besides, rGO@SBA is in well contact with PS with no obvious gaps. The wrinkled rGO can be found to embed into SBA microspheres. The segregated structure formed by the concentrated aggregation of rGO in the SBA is beneficial to the formation of micro capacitors. This is the possible reason why this segregated structure of rGO@SBA composite microspheres can significantly enhance the dielectric constant of the PS while their dielectric loss tangent is still in a low level. Fig. 5(b) shows the cross-sectional morphology of PS/rGO-SBA. Compared to the former, some gap between the filler and the matrix can be clearly seen (as shown by the arrow in the figure). Fig. 5(c) shows the cross-sectional morphology of PS/rGO, where the loss of the SBA has created more and wider gaps between the rGO and the PS matrix (as shown by the arrow in the figure).

Conclusions

This study determined the enhancement of the dielectric constant of PS by using rGO@SBA composite microspheres. The conclusions are as followed: (1) rGO significantly enhanced the dielectric constant of the SBA copolymer, with 1925 times higher than that of pure SBA in the dielectric permittivity (at 1 KHz) when the filling level was 2%. (2) At a very low loading of rGO@SBA (0.39 wt%), the dielectric permittivity of PS/rGO@SBA can be effectively increased, which is about three times that of PS/rGO-SBA, while the dielectric loss tangent of the composite is preserved at lower levels. (3) The rGO@SBA composite microspheres with a segregation structure have a better effect on improving the dielectric properties of PS matrix.

Conflicts of interest

There are no conflicts to declare.

Acknowledgements

This research was funded by Graduate Innovation Fund of Wuhan Institute of Technology (No CX2021157) and Guangdong Basic and Applied Basic Foundation (No 2019A1515110465). We also thank for the friendly technical support from Prof. Zhimin Dang, Tsinghua University.

References

1 Z. H. Dai, T. Li, Y. Gao, J. Xu, J. He, Y. Weng and B. H. Guo, *Compos. Sci. Technol.*, 2019, **169**, 142–150.
2 T. Chen, J. Qiu, K. Zhu, X. He, X. Kang and E. l. Dong, *Mater. Lett.*, 2014, **128**, 19–22.
3 N. V. Gorshkov, V. G. Goffman, M. A. Vikulova, I. N. Burmistrov, A. V. Kovnev and A. V. Gorokhovsky, *J. Compos. Mater.*, 2017, **52**, 135–144.
4 M. K. Mishra, S. Moharana, B. Behera and R. N. Mahaling, *Front. Mater. Sci.*, 2017, **11**, 82–91.
5 M. Ruan, D. Yang, W. Guo, L. Zhang, S. Li, Y. Shang, Y. Wu, M. Zhang and H. Wang, *Appl. Surf. Sci.*, 2018, **439**, 186–195.
6 Y. Wang, X. Chen, Y. Zhong, F. Zhu and K. P. Loh, *Appl. Phys. Lett.*, 2009, **95**, 063302.
7 Z. M. Dang, T. Zhou, S. H. Yao, J. K. Yuan, J. W. Zha, H. T. Song, J. Y. Li, Q. Chen, W. T. Yang and J. Bai, *Adv. Mater.*, 2009, **21**, 2077–2082.
8 B. Wang, G. Liang, Y. Jiao, A. Gu, L. Liu, L. Yuan and W. Zhang, *Carbon*, 2013, **54**, 224–233.
9 Z. M. Dang, S. H. Yao, J. K. Yuan and J. Bai, *J. Phys. Chem. C*, 2010, **114**, 13204–13209.
10 A. Javadi, Y. Xiao, W. Xu and S. Gong, *J. Mater. Chem.*, 2012, **22**, 830–834.
11 D. R. Wang, X. M. Zhang, J. W. Zha, J. Zhao, Z. M. Dang and G. H. Hu, *Polymer*, 2013, **54**, 1916–1922.
12 A. Dimiev, W. Lu, K. Zeller, B. Crowgey, L. C. Kempel and J. M. Tour, *ACS Appl. Mater. Interfaces*, 2011, **3**, 4657–4661.
13 W. Wu, X. Huang, S. Li, P. Jiang and T. Toshikatsu, *J. Phys. Chem. C*, 2012, **116**, 24887–24895.
14 W. Yang, S. Yu, R. Sun, S. Ke, H. Huang and R. Du, *J. Phys. D: Appl. Phys.*, 2011, **44**, 475305.
15 J. Lu, K. S. Moon, B. K. Kim and C. P. Wong, *Polymer*, 2007, **48**, 1510–1516.

16 X. Huang, Z. Zhou, G.-X. Chen and Q. Li, *Chem. Phys. Lett.*, 2018, **711**, 173–177.
17 D. Hu, M. Jiang, Y. Hou, J. Zhang, D. Fang, L. Liu, J. Huang, H. Li and C. Xiong, *J. Macromol. Sci., Part B: Phys.*, 2018, **57**, 255–265.
18 J. Yuan, Y. H. Lin, H. Lu, B. Cheng and C. W. Nan, *J. Am. Ceram. Soc.*, 2011, **94**, 1966–1969.
19 R. Ni, Q. Chen and X. Ding, *Polym. Compos.*, 2018, **39**, E1565–E1573.
20 D. He, Y. Wang, X. Chen and Y. Deng, *Composites, Part A*, 2017, **93**, 137–143.
21 Y. Feng, W. L. Li, J. P. Wang, J. H. Yin and W. D. Fei, *J. Mater. Chem. A*, 2015, **3**, 20313–20321.
22 X. Zhang, S. Zhao, F. Wang, Y. Ma, L. Wang, D. Chen, C. Zhao and W. Yang, *Appl. Surf. Sci.*, 2017, **403**, 71–79.
23 T. Wu, Y. Liu, X. Zeng, T. Cui, Y. Zhao, Y. Li and G. Tong, *ACS Appl. Mater. Interfaces*, 2016, **8**, 7370–7380.
24 H. Sun, H. Zhang, S. Liu, N. Ning, L. Zhang, M. Tian and Y. Wang, *Compos. Sci. Technol.*, 2018, **154**, 145–153.
25 Y. Lu, W. Y. Wang, F. Xue, J.-h. Yang, X.-d. Qi, Z.-w. Zhou and Y. Wang, *Chem. Eng. J.*, 2018, **345**, 353–363.
26 Y. Zhang, Y. Wang, Y. Deng, M. Li and J. Bai, *ACS Appl. Mater. Interfaces*, 2012, **4**, 65–68.
27 F. Liang, L. Zhang, W. Z. Lu, Q. X. Wan and G. F. Fan, *Appl. Phys. Lett.*, 2016, **108**, 072902.
28 A. P. Sobha and S. K. Narayanankutty, *IEEE Trans. Nanotechnol.*, 2014, **13**, 835–841.
29 X. Jiang, P. Ma, C. Zhou, W. Zhu, F. You, C. Yao and F. Liu, *Polym. Compos.*, 2020, **41**, 1234–1241.
30 X. Chao, P. Wu, Y. Zhao, P. Liang and Z. Yang, *J. Mater. Sci.: Mater. Electron.*, 2015, **26**, 3044–3051.
31 S. D. Kim, W. L. Zhang and H. J. Choi, *J. Mater. Chem. C*, 2014, **2**, 7541–7546.